Supporting information for:

Physicochemical Characteristics and Droplet Impact Dynamics of Superhydrophobic Carbon Nanotube Arrays

*Adrianus I. Aria† and Morteza Gharib**

Graduate Aeronautical Laboratories, California Institute of Technology, Pasadena, California 91125, United States

Table S1. Fabrication techniques and hydrophobicity parameters of various superhydrophobic surfaces.

Surfaces	Main fabrication technique	Surface modification technique	CA[a]	CAH / ROA[b]	H*[c]
CNT (this study)	PVD + CVD	Vacuum annealing	171	3	7.5×10^{7}
Si nanoparticles[1-3]	Sol-gel	Sol gel	165–173	3	1.4×10^{5}–1.6×10^{6}
Si nanopillars[4-6]	PVD + photolithography + RIE	CVD	154–165	1	1.1×10^{5}–9×10^{5}

CNT[7-10]	PVD + CVD	CVD	173–180	1	$4.5x10^4$–$3.3x10^5$
Polybutadiene[11]	Sol-gel	CVD	174	1	$4.5x10^4$
Polymer fibers[12-13]	Electrospinning or sol-gel	Sol-gel	165–180	0	$2.5x10^2$–$3.2x10^4$
Si micropillars[13-15]	PVD + photolithography + RIE	CVD	157–176	0–5	$1x10^3$–$1.5x10^3$
Lotus leaf[16]	N/A	N/A	155		$1.8x10^2$

a. Contact angle

b. Contact angle hysteresis / roll-off angle

c. Dimensionless robustness parameter[16]

DROPLET IMPACT PARAMETER SPACE

There are several important parameters governing the nature of impinging droplet that have to be taken into account. Those parameters are the droplet diameter (d_i), density (ρ), dynamic viscosity (μ) and surface tension (σ) of the liquid, impact velocity (v_i) of the droplet and the external air pressure. To make the analysis simpler, these parameters are represented by several important dimensionless numbers: Weber number (We), Reynolds number (Re), Ohnesorge number (Oh), Froude number (Fr), Bond number (Bo), and Capillary number (Ca). Weber number is defined as $We = \rho v_i^2 d_i/\sigma$. Reynolds number is defined as $Re = \rho v_i d_i /\mu$. Ohnesorge number is defined as $Oh = \mu/\sqrt{\rho\sigma\, d_i} = \sqrt{We}/Re$. Froude number is defined as $Fr = v_i^2/g d_i$. Bond number is defined as $Bo = \rho g d_i^2/\sigma$. Capillary number is defined as $Ca = \mu v_i/\sigma$. In this work, Weber number was varied from We=1.79 to We=335.32, which proportional to Reynolds number from Re = 529.64 to Re = 10,701.23. This broad range of Weber number was achieved by varying the initial droplet size from d_i = 2.2 mm to d_i = 3.8 mm and impact velocity from v_i =

0.24 m/s to v_i = 2.51 m/s, using DI water with a density of $\rho \approx 997$ kg/m^3 and a surface tension of $\sigma \approx 0.072$ N/m.

The effect of viscosity to the droplet can be considered to be minimal since the Ohnesorge number of experiment was found to be $1.71\text{x}10^{-3} \leq Oh \leq 2.52\text{x}10^{-3}$. In addition, the Froude, Bond, and Capillary number were set to be $2.24 \leq Fr \leq 229.22$, $0.65 \leq Bo \leq 2.02$, and $3.37\text{x}10^{-3} \leq Ca \leq 3.13\text{x}10^{-2}$, respectively. This condition implies the following: the effect of inertia is stronger than that of gravity, the effect of gravity is comparable to that of surface tension, and the effect viscosity is much less than that of surface tension. Further, the ratio between Bond and capillary numbers was found to be much larger than unity in each experiment. This ratio, which is defined as $Bo/Ca = \rho g d_i^2 / \mu v_i$, compares the effect of gravity and viscosity to the water droplet. Consequently, the effect of viscosity is also insignificant compared to the effect of gravity. Therefore, the impact behavior can be conveniently expressed just by Weber number. Weber number is considered as the most important parameter mainly because of its appearance in the energy balance of the droplet, which has been discussed in detail elsewhere,[17-23] and to avoid competition between two main components of kinetic energy, i.e. v_i and d_i. All of these dimensionless parameters are summarized in **Table S2**.

Table S2. Dimensionless parameters of the experiment.

	We	Re	Oh	Fr	Bo	Ca	Ba/Ca
Min	1.79	529.64	$1.71\text{x}10^{-3}$	2.24	0.65	$3.37\text{x}10^{-3}$	21.14
Max	335.32	10,701.23	$2.52\text{x}10^{-3}$	229.22	2.02	$3.13\text{x}10^{-2}$	287.99

DROPLET PINNING

Although no droplet pinning on the surface of the SH-CNT array is ever observed during the experiments, it does not necessarily mean that the droplet will never get pinned on the SH-CNT array. This actually suggests that the critical Weber number where droplet pinning takes place may be much smaller than We=1.79. In the very low We regime, the pinning Weber number (We_0),[24] can be roughly approximated as following:

$$We_0 = 12\,|\cos\theta_A - \cos\theta_R| \qquad 1$$

with θ_A and θ_R indicate the advancing and receding contact angles respectively. For SH-CNT array with θ_A = 173° and θ_R = 166°,[25] the pinning Weber number may be found around We_0 = 0.27, which is about an order of magnitude lower than the lowest We performed in this current study. This We_0 approximation is in fact similar to that observed on a CNT-coated micropatterned silicon surface where it was found that We_0 = 0.1.[15]

It has been hypothesised that partial pinning phenomenon in the high We regime occurs when the Laplace pressure (P_L) of the deformed liquid-vapor interface is higher than the dynamic pressure (P_D) of the impinging water droplet, but at the same time smaller than the effective water hammer pressure (P_{WH}) of the impinging water droplet $P_{WH} > P_L > P_D$.[26-27\15, 28] The Laplace pressure of the liquid-air interface can be written as:[28]

$$P_L = -\frac{2\sqrt{2}\sigma\cos\theta_A}{L} \qquad 2$$

with L is the intertube spacing of the SH-CNT array. The dynamic pressure of the droplet (P_D), is given by:

$$P_D = \frac{1}{2}\rho v_i^2 \quad (3)$$

with v_i is the impact velocity of the droplet. The effective water hammer pressure of the droplet (P_{WH}) is given by:

$$P_{WH} = 0.2\rho C v_i^2 \quad (4)$$

with C is the sound velocity in water, which in this case C ≈ 1497 m/s.

Using **Eq. 2**, the Laplace pressure of the liquid-air interface on the SH-CNT array with L ≈ 40 nm is calculated to be $P_L \approx 5$ MPa. Using **Eq.3**, the maximum dynamic pressure of the impinging water droplet is calculated to be $P_D \approx 3.1$ kPa. Using **Eq.4**, the maximum water hammer pressure of the impinging water droplet is calculated to be $P_{WH} \approx 0.75$ MPa. Since in this case $P_L > P_{WH} >> P_D$, the SH-CNT array is always in the total non-wetting state.[28] This prediction is in a good agreement with the experimental result where no droplet pinning has ever been observed on the SH-CNT array, even at a very high impact velocity of $v_i = 2.51$ m/s (equivalent to We = 335.32). Since droplet partial pinning occurs when $P_{WH} = P_L$, the pinning velocity can be predicted by combining **Eq.2** and **Eq.4**. On the other hand, since total wetting occurs when $P_D = P_L$, the total wetting velocity can be predicted by combining **Eq.2** and **Eq.4**. Based on the actual dimensions of SH-CNT arrays, with L = 40 nm, the water droplet partial pinning and total wetting are predicted to occur at an impact velocity of v_i =4.1 m/s and v_i = 100.7 m/s respectively.

SPREADING FACTOR

Based on the energy conservation approach, the droplet's energy balance during the free fall, impingement, and rebound phases is given by:

$$KE_1 + SE_1 = KE_2 + SE_2 + W_{12} \quad (5)$$

$$KE_2 + SE_2 - W_{23} = KE_3 + SE_3 \quad (6)$$

Eq.5 represents the droplet's energy balance during the free fall and spreading phases, while **Eq.6** represents the droplet's energy balance during the retraction and rebound phases. KE_1 and SE_1 are the droplet's kinetic energy and surface energy respectively during the free fall phase right before the impact. KE_2 and SE_2 are the droplet's kinetic energy and surface energy respectively when it reaches its maximum spreading diameter during the impingement. KE_3 and SE_3 are the droplet's kinetic energy and surface energy respectively during the rebound phase right after the impact. The loss of energy due to viscous dissipation when the droplet spreads and retracts on the surface during the impact are denoted by W_{12} and W_{23}, respectively. When the impinging droplet reaches its maximum diameter, the droplet's kinetic energy can be assumed to be negligible $KE_2 = 0$, because the velocity of the droplet is basically zero at that instant.

If it is assumed that the loss of energy due to viscous dissipation during the spreading and retraction phase is equal, $W_{12} = W_{23} = W$, **Eq.5** and **Eq.6** can be written in a single equation as:

$$KE_1 + SE_1 = KE_3 + SE_3 + 2W \quad (7)$$

where the kinetic energy of the droplet during the free fall and rebound phases is given by

$$KE_1 = \frac{1}{6}\pi\rho d_i^3 v_i^2 \quad (8)$$

$$KE_3 = \frac{1}{6}\pi\rho d_r^3 v_r^2 \quad (9)$$

and the surface energy of the droplet during the free fall and rebound phases is given by

$$SE_1 = \pi d_i^2 \sigma \quad (10)$$

$$SE_3 = \pi d_r^2 \sigma \quad (11)$$

After substituting **Eq.8**, **Eq.9**, **Eq.10**, **Eq.11**, into **Eq.7**, the loss of energy can be written as:

$$W = \frac{1}{12}\pi\rho(d_i^3 v_i^2 - d_r^3 v_r^2) + \frac{1}{2}\pi\sigma(d_i^2 - d_r^2) \quad (12)$$

Since $v_r = \varepsilon v_i$ and it can be assumed that $d_r \sim d_i$, **Eq.12** can be rewritten as:

$$W = \frac{1}{12}\pi\rho d_i^3 v_i^2 (1 - \varepsilon^2) \quad (13)$$

where ε is the coefficient of restitution of the impinging droplet.

The droplet's surface energy when it reaches its maximum spreading diameter can be expressed as:[20]

$$SE_2 = \pi\sigma d_s l_s + \frac{\pi}{4}\sigma(d_s - l_s)^2(1 - \cos\theta_s) \quad (14)$$

where l_s and θ_s are the thickness and the equilibrium contact angle of the droplet when it reaches its maximum spreading diameter (d_s). Experimental data show that the thickness of the droplet when it reaches its maximum diameter decreases rapidly as the increase of Weber number. At small Weber number, $We < We_1$, the droplet's thickness is still comparable to the maximum diameter of the droplet. However, at a moderate Weber number, $We_1 \leq We < We_2$, the droplet's thickness becomes an order of magnitude smaller than its maximum diameter. At even larger Weber number, $We \geq We_2$, the droplet's thickness is found to be $l << d_s$ and can no longer be observed. Since the first term of **Eq.14** is smaller than the second term, it is reasonable to drop the first term from **Eq.14**.[21, 23]. In addition, for superhydrophobic surfaces with $\theta_s \geq 150°$, the value of $\cos\theta_s$ is close to unity. Consequently, **Eq.14** can be approximated as:

$$SE_2 = \pi d_s \sigma \quad (15)$$

By substituting **Eq.8**, **Eq.10**, **Eq.13**, and **Eq.15** into **Eq.5**, the energy balance before the impinging droplet reaches its maximum spreading diameter can be written as:

$$\frac{1}{6}\pi\rho d_i^3 v_i^2 + \pi d_i^2 \sigma = \pi d_s^2 + \frac{1}{12}\pi\rho d_i^3 v_i^2 (1 - \varepsilon^2) \quad 16$$

Since $\beta = d_s / d_i$ and $We = \rho d_i v_i / \sigma$\$, **Eq.16** can be simplified as:

$$\beta = \left[\frac{1}{12} We (1 + \varepsilon^2) + 1\right]^{1/2} \quad 17$$

where β is the spreading factor of the impinging droplet. Compared to other published models of β,[21, 23, 29], the model given by **Eq.17** gives the best agreement to the experimental data (**Figure S4**).

Corresponding Author

* to whom correspondence should be addressed: mgharib@caltech.edu (M.G.).

REFERENCES

1. Ebert, D.; Bhushan, B. Transparent, Superhydrophobic, and Wear-Resistant Coatings on Glass and Polymer Substrates Using SiO2, ZnO, and ITO Nanoparticles. *Langmuir* **2012**, *28*, 11391-11399.
2. Boinovich, L.; Emelyanenko, A. M.; Pashinin, A. S. Analysis of Long-Term Durability of Superhydrophobic Properties under Continuous Contact with Water. *ACS Appl. Mater. Interfaces* **2010**, *2*, 1754-1758.
3. Manca, M.; Cannavale, A.; De Marco, L.; Aricò, A. S.; Cingolani, R.; Gigli, G. Durable Superhydrophobic and Antireflective Surfaces by Trimethylsilanized Silica Nanoparticles-Based Sol−Gel Processing. *Langmuir* **2009**, *25*, 6357-6362.
4. Ahuja, A.; Taylor, J. A.; Lifton, V.; Sidorenko, A. A.; Salamon, T. R.; Lobaton, E. J.; Kolodner, P.; Krupenkin, T. N. Nanonails: A Simple Geometrical Approach to Electrically Tunable Superlyophobic Surfaces. *Langmuir* **2007**, *24*, 9-14.
5. Deng, X.; Mammen, L.; Butt, H.-J.; Vollmer, D. Candle Soot as a Template for a Transparent Robust Superamphiphobic Coating. *Science* **2012**, *335*, 67-70.

6. Ma, Z. B.; Jiang, C. Y.; Li, X. M.; Ye, F.; Yuan, W. Z. Controllable fabrication of periodic arrays of high-aspect-ratio micro-nano hierarchical structures and their superhydrophobicity. *J. Micromech. Microeng.* **2013**, *23*.
7. Lau, K.; Bico, J.; Teo, K.; Chhowalla, M.; Amaratunga, G.; Milne, W. Superhydrophobic carbon nanotube forests. *Nano Lett.* **2003**, *3*, 1701-1705.
8. Huang, L.; Lau, S.; Yang, H.; Leong, E.; Yu, S.; Prawer, S. Stable superhydrophobic surface via carbon nanotubes coated with a ZnO thin film. *J. Phys. Chem. B* **2005**, *109*, 7746-7748.
9. Hong, Y.; Uhm, H. Superhydrophobicity of a material made from multiwalled carbon nanotubes. *Appl. Phys. Lett.* **2006**, *88*, 244101-1-244101-3.
10. Cho, S.; Hong, Y.; Uhm, H. Hydrophobic coating of carbon nanotubes by CH4 glow plasma at low pressure, and their resulting wettability. *J. Mater. Chem.* **2007**, *17*, 232-237.
11. Brown, P. S.; Berson, A.; Talbot, E. L.; Wood, T. J.; Schofield, W. C. E.; Bain, C. D.; Badyal, J. P. S. Impact of Picoliter Droplets on Superhydrophobic Surfaces with Ultralow Spreading Ratios. *Langmuir* **2011**, *27*, 13897-13903.
12. Gao, L.; McCarthy, T. A perfectly hydrophobic surface (theta(A)/theta(R)=180 degrees/180 degrees). *J. Am. Chem. Soc.* **2006**, *128*, 9052-9053.
13. Tuteja, A.; Choi, W.; Ma, M.; Mabry, J. M.; Mazzella, S. A.; Rutledge, G. C.; McKinley, G. H.; Cohen, R. E. Designing Superoleophobic Surfaces. *Science* **2007**, *318*, 1618-1622.
14. Gao, L.; McCarthy, T. The "lotus effect" explained: Two reasons why two length scales of topography are important. *Langmuir* **2006**, *22*, 2966-2967.
15. Chen, L.; Xiao, Z.; Chan, P. C. H.; Lee, Y.-K.; Li, Z. A comparative study of droplet impact dynamics on a dual-scaled superhydrophobic surface and lotus leaf. *Appl. Surf. Sci.* **2011**, *257*, 8857-8863.
16. Tuteja, A.; Choi, W.; McKinley, G. H.; Cohen, R. E.; Rubner, M. F. Design Parameters for Superhydrophobicity and Superoleophobicity. *MRS Bull.* **2008**, *33*, 752-758.
17. Chandra, S.; Avedisian, C. On the collision of a droplet with a solid surface. *P. R. Soc. A* **1991**, *432*, 13-41.
18. Pasandideh-Fard, M.; Qiao, Y. M.; Chandra, S.; Mostaghimi, J. Capillary effects during droplet impact on a solid surface. *Phys. Fluids* **1996**, *8*, 650-659.
19. Kim, H. Y.; Chun, J. H. The recoiling of liquid droplets upon collision with solid surfaces. *Phys. Fluids* **2001**, *13*, 643-659.
20. Ukiwe, C.; Kwok, D. Y. On the Maximum Spreading Diameter of Impacting Droplets on Well-Prepared Solid Surfaces. *Langmuir* **2004**, *21*, 666-673.
21. Vadillo, D.; Soucemarianadin, A.; Delattre, C.; Roux, D. Dynamic contact angle effects onto the maximum drop impact spreading on solid surfaces. *Phys. Fluids* **2009**, *21*, 122002-1-122002-8.
22. Li, R.; Ashgriz, N.; Chandra, S. Maximum Spread of Droplet on Solid Surface: Low Reynolds and Weber Numbers. *J. Fluid Eng.-T. ASME* **2010**, *132*, 061302-1-061302-5.
23. Lee, J.; Lee, S. Dynamic Wetting and Spreading Characteristics of a Liquid Droplet Impinging on Hydrophobic Textured Surfaces. *Langmuir* **2011**, *27*, 6565-6573.
24. Rioboo, R.; Voue, M.; Vaillant, A.; De Coninck, J. Drop Impact on Porous Superhydrophobic Polymer Surfaces. *Langmuir* **2008**, *24*, 14074-14077.
25. Aria, A. I.; Gharib, M. Reversible Tuning of the Wettability of Carbon Nanotube Arrays: The Effect of Ultraviolet/Ozone and Vacuum Pyrolysis Treatments. *Langmuir* **2011**, *27*, 9005-9011.

26. Reyssat, M.; Pepin, A.; Marty, F.; Chen, Y.; Quere, D. Bouncing transitions on microtextured materials. *Europhys. Lett.* **2006**, *74*, 306-312.
27. Jung, Y.; Bhushan, B. Dynamic effects of bouncing water droplets on superhydrophobic surfaces. *Langmuir* **2008**, *24*, 6262-6269.
28. Deng, T.; Varanasi, K. K.; Hsu, M.; Bhate, N.; Keimel, C.; Stein, J.; Blohm, M. Nonwetting of impinging droplets on textured surfaces. *Appl. Phys. Lett.* **2009**, *94*, -.
29. Clanet, C.; Beguin, C.; Richard, D.; Quere, D. Maximal deformation of an impacting drop. *J. Fluid Mech.* **2004**, *517*, 199-208.

FIGURES

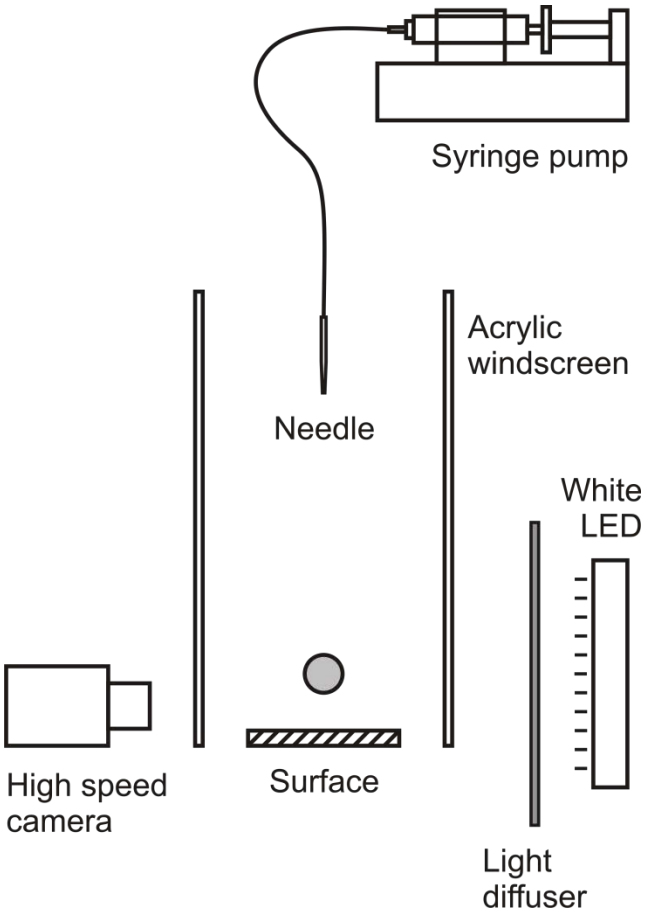

Figure S1. Schematic of the experimental setup.

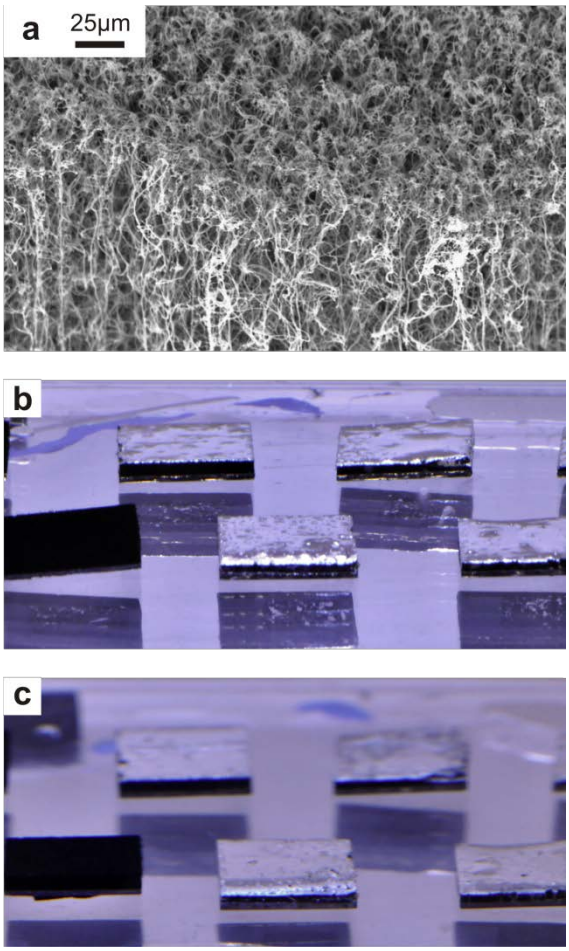

Figure S2. (a) High magnification scanning electron microscopy image of SH-CNT array after the droplet impact experiment at We ≈ 335. (b) Top view of AG-CNT array (bottom left) and SH-CNT arrays submerged in a deep pool of DI water. The AG-CNT array appears black while the SH-CNT arrays look reflective. (c) Top view of the same AG-CNT array and SH-CNT arrays two weeks later, showing the silvery appearance of the SH-CNT arrays. This confirms the capability of SH-CNT arrays to retain their Cassie state superhydrophobicity even after being continuously submerged in water for two weeks.

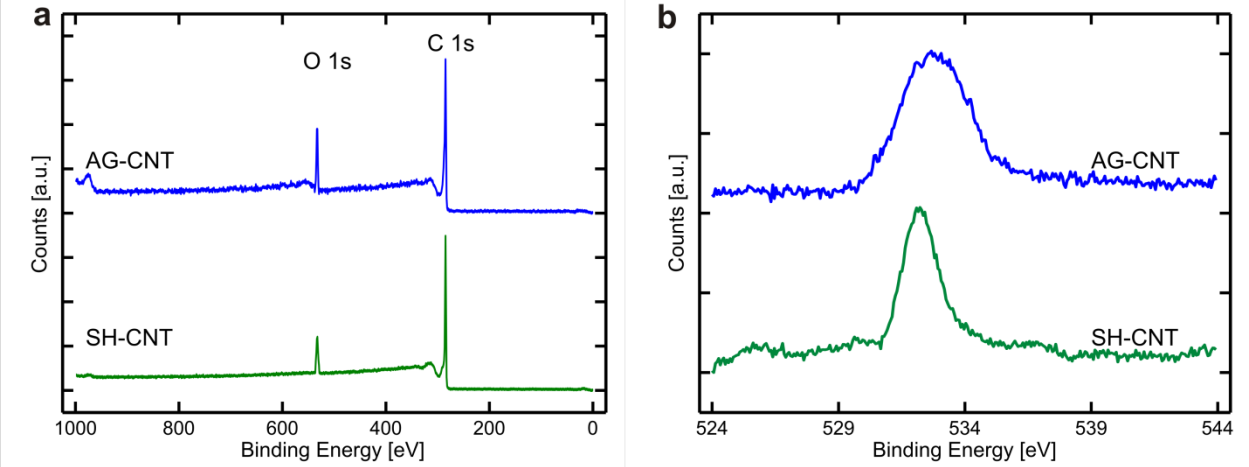

Figure S3. (a) Survey-scan XPS spectra of C1s and O1s peaks of AG-CNT and SH-CNT arrays used for calculating O/C ratio. (b) High-resolution XPS spectra of O1s peak of AG-CNT and SH-CNT arrays.

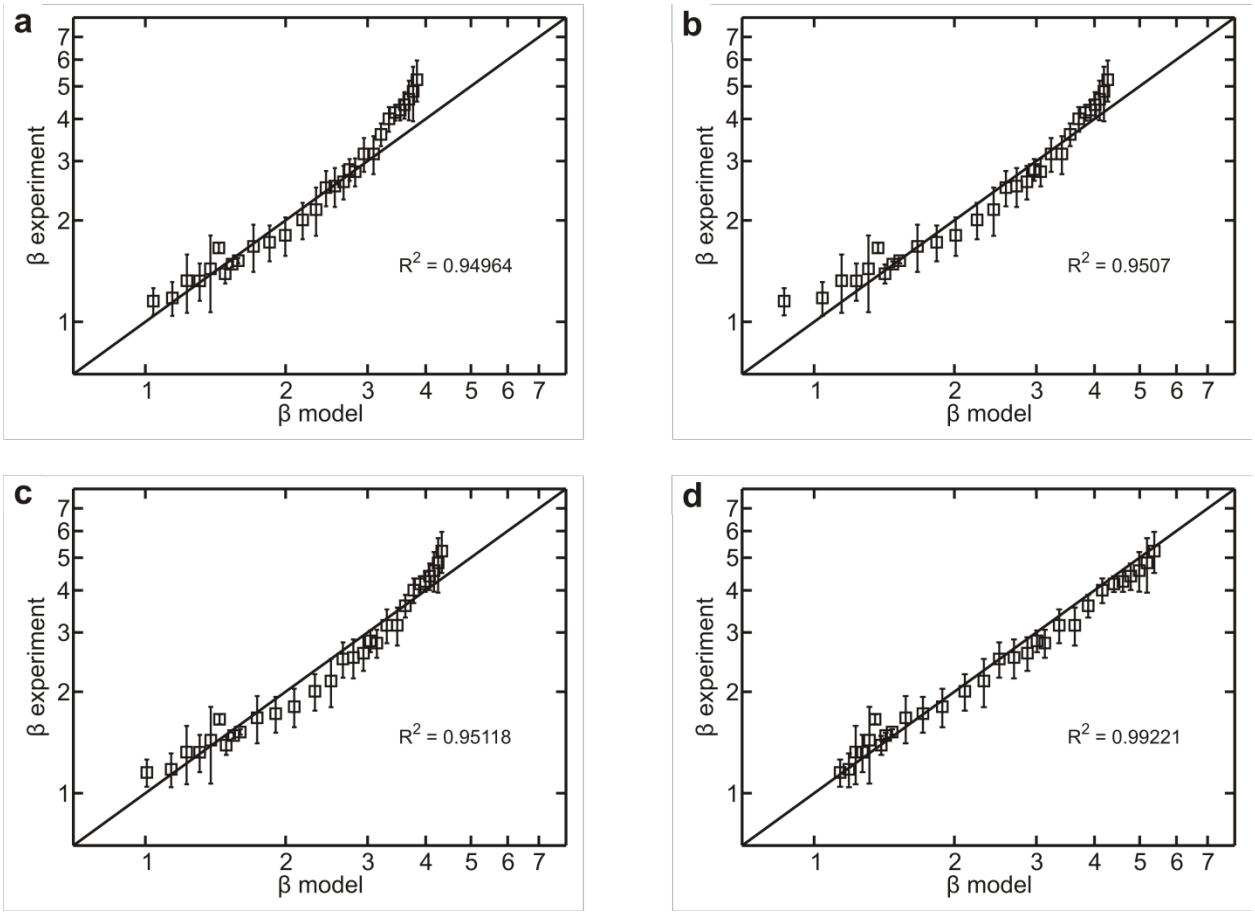

Figure S4. Correlation plot of β obtained from experimental observation and model prediction. The model for β is given by (a) Clanet et al.,[29] (b) Vadillo et al.,[21] (c) Lee and Lee,[23] (d) **Eq. 17**.

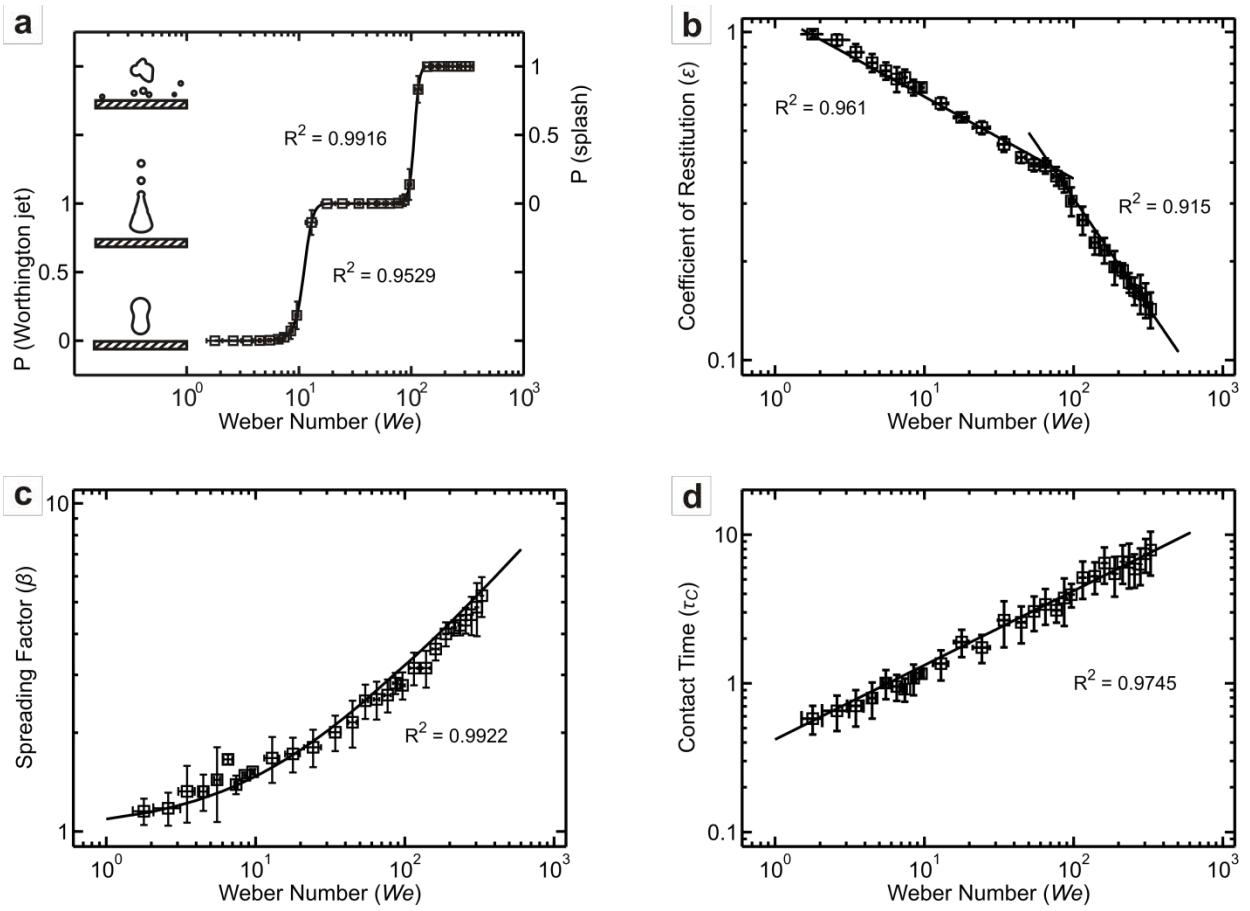

Figure S5. (a) Probability of a water droplet to create a Worthington jet or a prompt splash upon impact. Log-log plots of (b) ε, (c) β, and (d) τ_C as a function of We of the droplet. Markers indicate the mean data observed in the experiment and error bars indicate the standard deviation from the mean.